

THE INSTITUTE OF
SPACE AND ASTRONAUTICAL SCIENCE
REPORT NO.682

Computational Prediction of
the Aerodynamic Characteristics of SSTO
Vehicle Configurations

By

Keiichiro FUJIMOTO and Kozo FUJII

September 2003

The Institute of Space and Astronautical Science, Kanagawa

ISAS REPORT No.682 (September) 2003

Published The Institute of Space and Astronautical Science(ISAS)
3-1-1 Yoshinodai, Sagamihara, Kanagawa, 229-8510, Japan
Fax : +81-42-759-8440
E-mail : newsedit@adm.isas.ac.jp

Printed TAIYO-PRINTING CO.,LTD.
4-9-10 Kamimizo, Sagamihara, Kanagawa, 229-1123, Japan

The Institute of Space and Astronautical Science (ISAS)
publishes the ISAS Report to publicize its reserch activities at
irregular intervals. Copyrights to the ISAS Report belong to the ISAS.
All Communication relating to these reports should be addressed to
the Administration Department, General Affairs Division, ISAS.

Computational Prediction of the Aerodynamic Characteristics of SSTO Vehicle Configurations

By

Keiichiro FUJIMOTO and Kozo FUJII

(September 2003)

Abstract: Flow-fields around basic SSTO-rocket configurations are numerically simulated by the Navier-Stokes computations. The study starts with the simulations of the Apollo-type configuration, in which the simulated results are compared with NASA's experiments and the capability of CFD approach is discussed. Computed aerodynamic coefficients of Apollo configuration agree well with the experiments at subsonic, transonic and supersonic regime at all angles of attack and the present computational approach is validated. Effects of the configuration parameters on the aerodynamic characteristics are then numerically investigated and clarified in detail. It turns out that the aerodynamic characteristics of the body is mainly influenced by the location of the flow separation, the shock waves on the surface and the pressure level behind the body. The shoulder radius of the body has strong influence to the Mach number dependency of the aerodynamic characteristics. The fineness ratio of the body mainly influences to the lift characteristics.

Nomenclature

x, y, z	Cartesian body axes	C_N	Normal force coefficient, normal force/($q S_{ref}$)
u, v, w	Velocity components	C_D	Drag coefficient, drag/($q S_{ref}$)
	Density	C_L	Lift coefficient, lift/($q S_{ref}$)
e	Total energy per unit volume	L/D	Lift to drag ratio C_L/C_D
T	Temperature	C_{D0}	Zero-lift drag coefficient
p	Pressure	C_{ma}	pitching-moment coefficient computed about theoretical apex
q	Dynamic pressure		
D_{max}	Maximum diameter of the body		
S_{ref}	Reference area, frontal area of the body		
M	Mach number		
Re	Reynolds number based on D_{max}		
Pr	Prandtl number		
μ	Viscosity		
	Angle of attack, deg		
C_A	Axial force coefficient, axial force/($q S_{ref}$)		

Subscripts

$inf()$	freestream condition
max	maximum value
lam	laminar state value
tur	turbulent state value

1 INTRODUCTION

Current expendable launch vehicles (ELVs) and Shuttles are able to launch spacecraft, crews, and payloads needed for commercial and scientific purposes. However, the cost of the access to space is far too high, and reliability and operability of the system fall short of desired levels. Considering these factors, next-generation space-launch vehicle is definitely needed to replace current ELVs. In the past twenty years, many concepts have been considered and studied aiming to reduce launch costs and improve the reliability and flexibility of space transportation systems. In 1994, NASA headquarters concluded that one option recommended for the access to space was a development of a fully reusable, all rocket propelled, Single-Stage-To-Orbit (SSTO) launch vehicle^[1]. With improved ground and flight operations, fully reusable SSTO rocket

system has the potential to fulfill the requirements as a space transportation system in the next generation.

Generally, there exist two concepts of such SSTO rocket system; vertical-takeoff/horizontal-landing (VTHL) and vertical-takeoff/vertical-landing (VTOL) concept. NASA developed X-33 as a technology demonstrator, designed as a VTHL-SSTO vehicle with a lifting body. On the other hand, as a VTOL, Delta Clipper - the experimental (DC-X and XA) vehicles have extensively demonstrated the re-usability of the SSTO rocket and the flight capability of VTOL vehicles. Unfortunately, all the activities were stopped due to the budget problem and technical difficulties (Fig. 1). At the Institute of Space and Astronautical Science (ISAS), ground and flight tests of the VTOL-SSTO rocket system are presently conducted for the establishment of the basic technologies^[2] (Fig. 2).

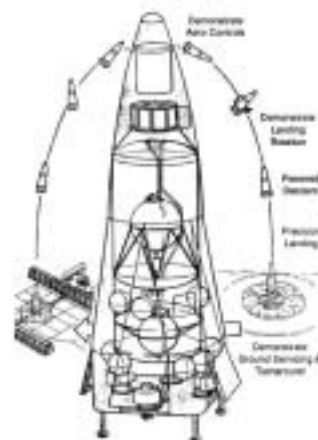
Since the configuration of such VTOL-SSTO rockets is totally different from conventional rocket configurations and its flight trajectory includes a wide range of flow conditions; subsonic through hypersonic and variety of attack angles, there should be various considerations for the vehicle's aerodynamics to realize atmospheric flight.

As shown in Fig. 3, there also exist two types of entry flight concepts; nose and base entry, each has its own advantage, aerodynamic analysis of such vehicles should include whole range of flow conditions. In addition, high lift-to-drag-ratios (L/D), high maneuverability is one of the key issues for the design of the vehicle's configuration as general VTOL-SSTO rocket has no wing on their body. However, there exist little aerodynamic data of such vehicles and even basic flow-fields have not been clarified.

In the preliminary design stage of the vehicle configuration, CFD analysis has strong advantages as it supplies a wide range of aerodynamic data, whereas only limited data can be obtained by the wind-tunnel experiments. CFD analysis is already an established essential tool in the design process of aircraft based on the fact that certain level of reliability has been established by the accumulation of the flow simulations. In the other fields, however, CFD reliability has not been established, and this is also true for the space launch vehicles. In the present paper the results of the CFD simulations for the aerodynamic analysis of basic SSTO configurations are presented. The research starts with the simulations of the subsonic, transonic and supersonic flow-field for the Apollo configuration at wide range of attack angles for the establishment of the CFD-approach reliability. Apollo configuration was chosen since there are large amount of experimental data available, although this configuration was designed only for entry flight and is not adequate as a SSTO rocket configuration. Capability of CFD estimation of the aerodynamic characteristics is discussed by the comparison with the NASA's experiments. Based on the confirmation of the reliability of the CFD approach, the effect of the configuration parameters is next discussed. The results show the effect of each parameter on the aerodynamic characteristics. The flow mechanisms behind the aerodynamic characteristics were also revealed.



(a) Flight testing.



(b) Schematic view of flight trajectory.

Figure 1: Delta Clipper Experimental (DC-X) http://www.hq.nasa.gov/office/pao/History/x-33/menu_dcx.htm.



(a) Flight testing.

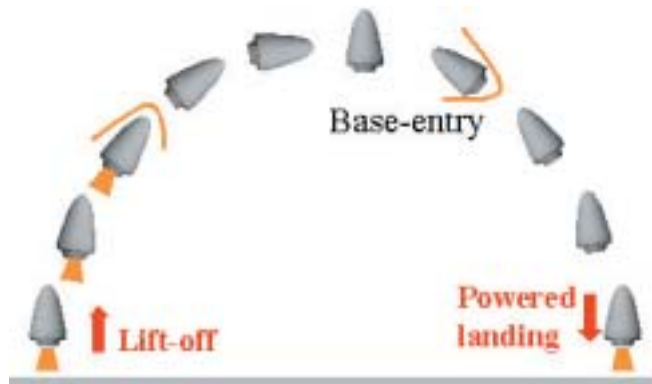


(b) Schematic view of flight trajectory.

Figure 2: Subscale VTOL testing vehicle.



(a) Nose first entry.



(b) Base first entry.

Figure 3: Concepts of the entry type.

2 Numerical Methods

2.1 Geometries

Body configuration considered in the present study is axisymmetric basic form as shown in Fig. 4, which has four configuration parameters; radius of the cone apex R_f , cone half-angle θ , shoulder radius R_s and diameter of the base sphere R . All body configurations are shown in Fig. 5. Three sets of configurations (set 01, set 02 and set 03) are considered and their configuration parameters are shown in Tables 2, 3 and 4, respectively. Set 01 is used for the investigation of the effect of the configuration parameters, R_f , R_s , and R on the aerodynamic characteristics, Set 02 is used for the effect of the R_s on the C_{D0} characteristics at $\alpha = 180^\circ$ and Set 03 is used for the effect of the R_s on the C_{D0} characteristics at $\alpha = 180^\circ$. All geometries are non-dimensionalized by the maximum diameter of the D_{max} .

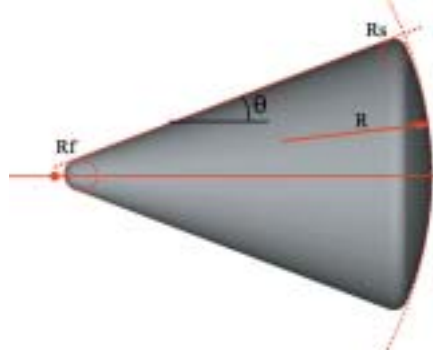


Figure 4: Definition of the configuration and the parameters.

2.2 Flow solver

Compressible Navier-Stokes Equations

The three-dimensional compressible (Favre-averaged) Navier-Stokes equations in the generalized coordinate system governing the flow of an unsteady, ideal gas can be written in the conservation-law form:

$$\frac{\hat{Q}}{t} + \frac{\hat{E}_{eul}}{x} + \frac{\hat{F}_{eul}}{y} + \frac{\hat{G}_{eul}}{z} = \frac{1}{Re_L} \frac{\hat{S}_{vis}}{x} \quad (1)$$

$$\hat{Q} = \frac{1}{J} \begin{bmatrix} u \\ v \\ w \\ e \end{bmatrix}$$

$$\hat{E}_{eul} = \frac{1}{J} \begin{bmatrix} U \\ uU + xP \\ vU + yP \\ wU + zP \\ (e+p)U - tP \end{bmatrix}, \quad \hat{F}_{eul} = \frac{1}{J} \begin{bmatrix} V \\ uV + xP \\ vV + yP \\ wV + zP \\ (e+p)V - tP \end{bmatrix}, \quad \hat{G}_{eul} = \frac{1}{J} \begin{bmatrix} W \\ uW + xP \\ vW + yP \\ wW + zP \\ (e+p)W - tP \end{bmatrix},$$

$$\hat{E}_{eul} = \frac{1}{J} \begin{bmatrix} 0 \\ \mu_{tot} m_{1W} + (\mu_{tot}/3) m_2 x \\ \mu_{tot} m_{1W} + (\mu_{tot}/3) m_2 y \\ \mu_{tot} m_{1W} + (\mu_{tot}/3) m_2 z \\ m_{1m3} + (\mu_{tot}/3) m_2 (x^u + y^v + z^w) \end{bmatrix}, \quad (2)$$

Here,

$$\begin{aligned} U &= t + x^u + y^v + z^w \\ V &= t + x^u + y^v + z^w \\ W &= t + x^u + y^v + z^w \end{aligned} \quad (3)$$

$$\begin{aligned} \mu_{tot} &= \mu_l + \mu_t \\ m_1 &= x^2 + y^2 + z^2 \\ m_2 &= x^u + x^v + x^w \\ m_3 &= \mu_{tot} (u^2 + v^2 + w^2) / 2 + \frac{1}{\gamma - 1} \left(\frac{\mu_{lam}}{Pr_{lam}} + \frac{\mu_{tur}}{Pr_{tur}} \right) c^2 \end{aligned} \quad (4)$$

Length, and velocity components u, v, w are normalized by D_{max} , and c , respectively.

For high-Reynolds-number flows, the viscous effects are confined to a thin layer near the wall boundary and are dominated by the viscous terms associated with the strain rates normal to the wall. The terms associated with the strain rates along the body surface are comparatively small and negligible. Also, since the computational grid is highly concentrated near the body surface, resulting in the mesh aspect ratio becoming very large, the inclusion of these terms would not change the solution. Thus, the thin-layer approximation has been introduced in Eqs. (1), as is typically done in most of the Navier-Stokes computations in the past.

Compressible flow closure approximations are achieved by using Molkovin's hypothesis. The pressure, density and velocity components are related to the energy for an ideal gas by the following equation:

$$p = \left(\gamma - 1 \right) \left\{ e - \frac{1}{2} (u^2 + v^2 + w^2) \right\} \quad (5)$$

The metrics are evaluated using second-order central-difference formulas for the interior-points.

Numerical fluxes for the convective terms are evaluated by the SHUS scheme (Simple High-resolution Upwind Scheme)^[3], extended to high-order space accuracy by the 3rd-order upwind-biased MUSCL interpolation^[4] based on the primitive variables. The viscous terms are evaluated by the 2nd-order central differencing. The LU-ADI factorized implicit algorithm^[5] is used for the time integration, and inner iterations are not used.

The flow-field is considered to be fully turbulent, and the Baldwin-Lomax's algebraic turbulence model^[6] (BL-model) with the Degani-Schiff's modification^[7] is applied. Note that this popular turbulence model is intentionally used as the objective of the present paper includes the assessment of the prediction capability of the conventional CFD method.

Detached Eddy Simulation (DES)^[9] versions of Spalart-Allmaras one equation turbulence model^[8] (SA-DES model) is applied for the investigation of the effects of the turbulence model. In the DES analysis the distance from the wall d in the SA-model is replaced by

$$\tilde{d} = \min(d, C_{DES} \Delta) \quad (6)$$

Where Δ is maximum grid spacing size defined as $\Delta = \max(\Delta x, \Delta y, \Delta z)$. When $d \ll \Delta$, the model acts in a RANS mode and when $d \gg \Delta$ the model acts in a Smagorinski LES mode. Original constant value of $C_{DES} = 0.65$ is used in the present study.

2.3 Computational Domain and Grid

The flow-fields are assumed to be symmetric about the pitch-plane ($y=0$). Therefore, the computational domain covers only half of the body. The computational mainly grid used in this study is Grid 01, $91 \times 53 \times 61$ with O-O topology, as shown in Fig. 6. This small grid size is intentionally used since one of the main purpose is to assess the capability of CFD where large number of cases could be simulated under the standard computer environment. Other two computational grids, Grid 02 and Grid 03 are used for the grid resolution study. The details of the computational grids are shown in the Tab. 1. The minimum grid spacing near the wall is 3.0×10^{-5} and the computational domain ranges from -10.0 to +10.0 in all directions as shown in Fig. 7.

2.4 Body system of axes

As shown in Fig. 8, $\alpha = 180^\circ$ corresponds to the base entry and $\alpha = 0^\circ$ corresponds to the nose entry. An anti-clockwise rotation corresponds to the direction of decreasing angles of attack. The pitching-moment coefficient C_{ma} is computed about the theoretical apex. The definition of the aerodynamic forces are shown in Fig. 8.

Table 1: Details of computational grids.

Grid-Name	Minimum grid spacing	(-dir, -dir, -dir)	total grid points
Grid01	3.0×10^{-5}	(91 × 53 × 61)	294203 pts.
Grid02	3.0×10^{-5}	(131 × 83 × 116)	1261268 pts.
Grid03	3.0×10^{-5}	(171 × 53 × 165)	1495395 pts.

2.5 Flow parameters

Since the variation range of μ_{lam} is small as compared to μ_t which is shown in the previous studies, μ is fixed 1.0 in all the computations. Mach number ranges from 0.6 through 2.0, the angle of attack ranges from 0.0 through 180 °Reynolds number is 1.0×10^6 . Consideration of the subsonic to supersonic aerodynamic characteristics is important for the preliminary design stage, therefore aerodynamic characteristics in this speed regime is especially focused on. Pr_{lam} , Pr_{tur} and μ_{lam} are fixed 0.72, 0.90 and 1.0 in the present computations.

2.6 Data processing

All of the aerodynamic coefficients in the following discussions are time-averaged physical variables obtained by the computations using local time stepping technique. The aerodynamic forces of the body are strongly influenced by the flow unsteadiness behind the body. The lee-side pressure varies in time due to the unsteady re-circulating wake flow behind the body. Even with the local time stepping, the flow unsteadiness still remains. Therefore the results are averaged in time. Our experience for wide variety of the flow simulations in the past showed that it is acceptable for the flow-fields that does not include complicated flow structure. The estimated lee-side pressure behind the body tends to be slight higher in the computations using the local time stepping technique.

Table 2: Configuration parameters compared with Apollo (set 01).

case	R	rs	rf		L_b	L_b/D_{max}
Apollo	1.195(1.0)	0.05(1.0)	0.0594(1.0)	33.0	0.831(1.000)	1.662(1.000)
case 1	1.195(1.0)	0.05(1.0)	0.1140(2.0)	33.0	0.877(1.055)	1.754(1.055)
case 2	1.195(1.0)	0.25(5.0)	0.1140(2.0)	33.0	1.032(1.242)	2.064(1.242)
case 3a	1.195(1.0)	0.05(1.0)	0.1140(2.0)	21.0	1.249(1.503)	2.498(1.503)
case 3b	1.195(1.0)	0.05(1.0)	0.0594(1.0)	21.0	1.348(1.622)	2.695(1.622)
case 4a	1.195(1.0)	0.10(2.0)	0.1140(2.0)	33.0	0.880(1.059)	1.759(1.059)
case 4b	1.195(1.0)	0.10(2.0)	0.0594(1.0)	33.0	0.926(1.114)	1.851(1.114)

Table 3: Configuration parameters of Case 3a-1 ~ 3a-4 compared with Apollo (set 02).

case	R	rs	rf		L_b	L_b/D_{max}
Apollo	1.195(1.0)	0.05(1.0)	0.0594(1.0)	33.0	0.831(1.000)	1.662(1.000)
case 3a	1.195(1.0)	0.05(1.0)	0.1140(2.0)	21.0	1.249(1.503)	2.498(1.503)
case 3a-1	1.195(1.0)	0.10(2.0)	0.1140(2.0)	21.0	1.293(1.556)	2.586(1.556)
case 3a-2	1.195(1.0)	0.15(3.0)	0.1140(2.0)	21.0	1.337(1.609)	2.674(1.609)
case 3a-3	1.195(1.0)	0.20(4.0)	0.1140(2.0)	21.0	1.382(1.663)	2.764(1.663)
case 3a-4	1.195(1.0)	0.25(5.0)	0.1140(2.0)	21.0	1.428(1.718)	2.856(1.718)

Table 4: Configuration parameters of Apollo, Case 5, Case 3b and Case 6 (set 03).

case	R	rs	rf		L_b	L_b/D_{max}
Apollo	1.195(1.0)	0.05(1.0)	0.0594(1.0)	33.0	0.831(1.000)	1.662(1.000)
Case 5	1.195(1.0)	0.05(1.0)	0.0594(1.0)	27.0	1.064(1.280)	2.128(1.280)
case 3b	1.195(1.0)	0.05(1.0)	0.0594(1.0)	21.0	1.348(1.622)	2.695(1.622)
Case 6	1.195(1.0)	0.05(1.0)	0.0594(1.0)	15.0	1.845(2.220)	3.689(2.220)

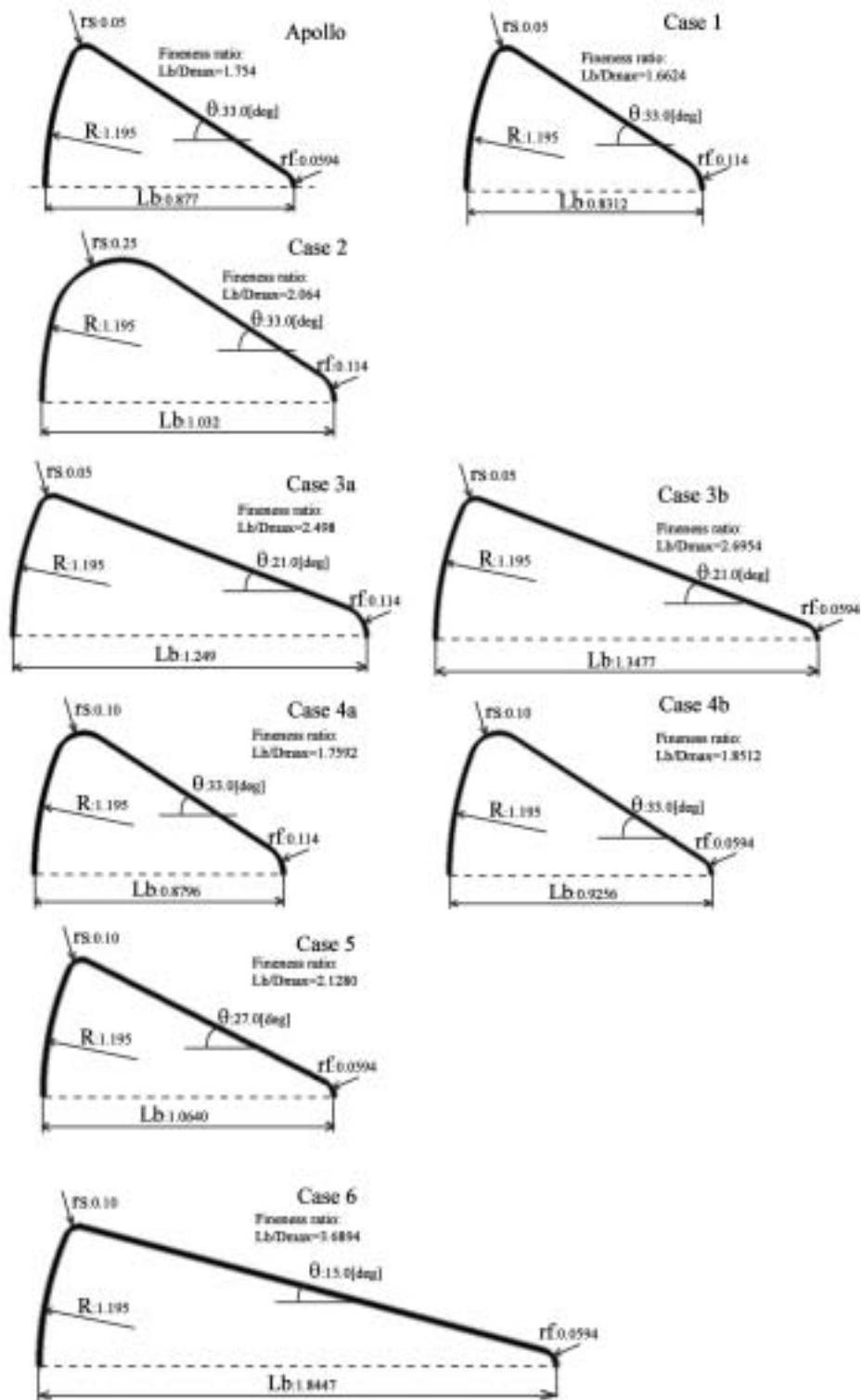


Figure 5: Configuration of the bodies.

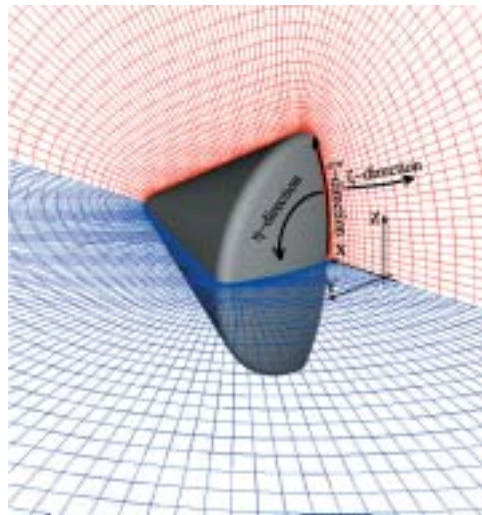


Figure 6: Entire view of the grid (Grid 01).

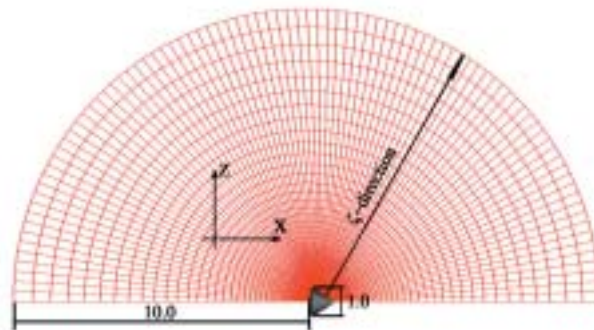


Figure 7: Entire view of the grid (Grid 01).

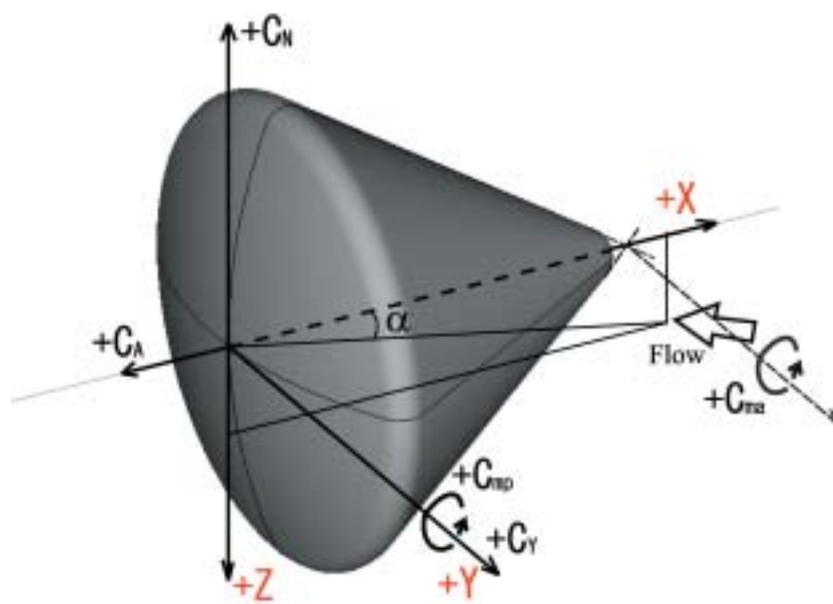


Figure 8: Sketch showing body system of axes.

3 Results and Discussion

3.1 CFD Validation and Discussion

CFD estimation of the aerodynamic characteristics for the Apollo at various freestream conditions are carried out, and compared with the experimental data^[10] for the validation of CFD approach. The freestream conditions used in the computations are shown in Table 5. All computations are carried out with constant Reynolds number 1.0×10^6 .

Although there exist some differences of the Reynolds number with the William et al experiment (Table 6), it was numerically shown that the effect on the aerodynamic characteristics is small since the viscous component of aerodynamic forces are much smaller than the pressure component.

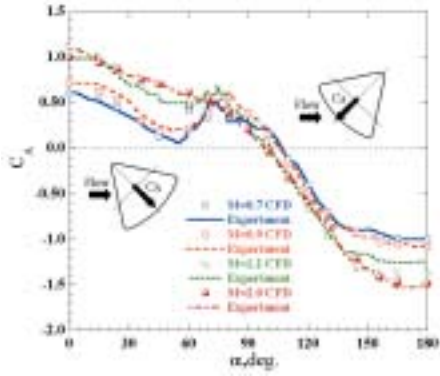
The aerodynamic coefficients are compared in Figs. 9(a)-9(c). The present CFD results are in excellent agreement with the experiments for all the angles of attack at whole speed regime expect for $M = 0.7$ with $\approx 100^\circ$. The discrepancies of the C_N and C_{ma} tend to be smaller when M increases. Under the condition of subsonic flow with high angles of attack, the complicated viscous separation occurs on the inclined surface of the cone part as shown in Fig. 10(b). It is shown that the discrepancy mainly due to the poor grid resolution. The detailed description can be seen in the Appendix A. Some effect of the grid resolution and little effects of the turbulence model were observed at certain flow conditions. However for the preliminary stage of the configuration design, the computed results on the Grid 01 can be considered to be sufficiently reliable. The wind-tunnel experiments were conducted for the Apollo-like configurations. Although they are not shown here, the computed results for them are in reasonable agreement with the experimental data, maximum discrepancy is within 0.1 for all the configurations.

Table 5: Flow conditions.

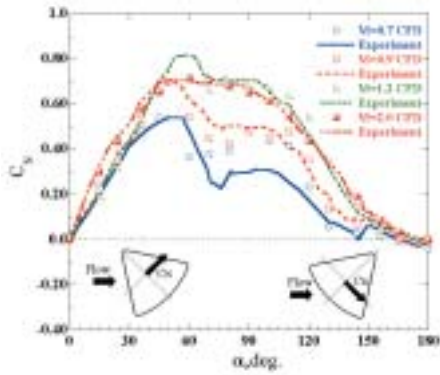
M	0.7, 0.9, 1.2, 2.0
Re	1.0×10^6
	0, 15, 24, 36, 45, 60, 70, 80, 90, 100, 110, 120, 130, 144, 156, 165, 180°

Table 6: Flow conditions for William et al 's exp

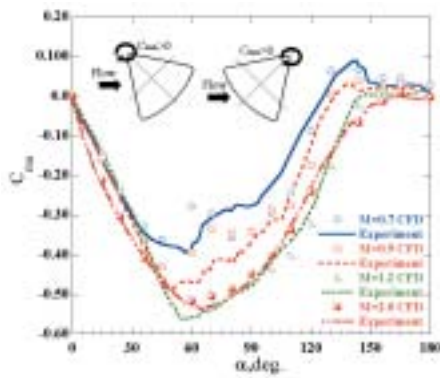
M	0.7, 0.9, 1.2, 2.0
Re	3.9, 3.3, 2.8, 3.6×10^6



(a) Axial force coefficients C_A .



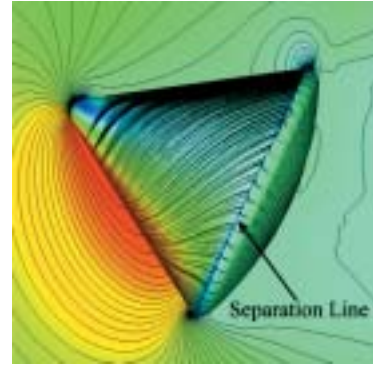
(b) Normal force coefficients C_N .



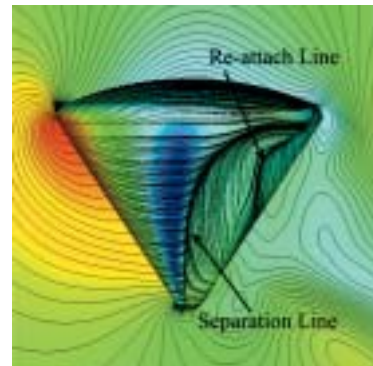
(b) Normal force coefficients C_N .



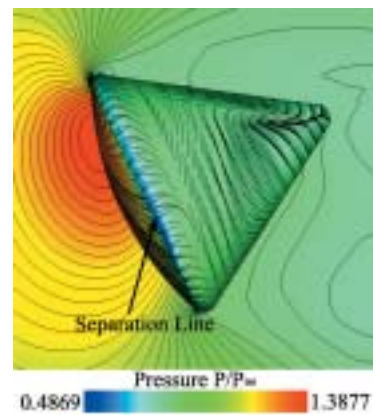
Figure 9: Computed aerodynamic coefficients for Apollo with experimental data^[10].



(a) Apollo at $M = 0.7$, $\alpha = 36^\circ$.



(b) Apollo at $M = 0.7$, $\alpha = 90^\circ$.



(c) Apollo at $M = 0.7$, $\alpha = 156^\circ$.

Figure 10: The computed p/p_∞ distributions and surface flow pattern for Apollo.

3.2 Effects of configuration parameters on the aerodynamic characteristics

Based on the results in the previous section, CFD simulation is used for the prediction of the aerodynamic forces and moments for other body configurations. The freestream conditions are shown in Table 7. Although the flow computations are carried out for $M = 0.7, 0.9, 1.2$ and 2.0 , the discussions are limited to two flow conditions, $M = 0.9$ and 1.2 . The computed aerodynamic coefficients for the Apollo, Case 2a and Case 3a against angles of attack are shown in Figs. 13 ~ 20 for each Mach number and in Figs. 21 ~ 27 for each geometry.

The influence of the radius of the cone apex, radius of the shoulder and the fineness ratio are discussed in the following sections.

3.2.1 Base-entry aerodynamics($\alpha = 90 \sim 180^\circ$)

Effect of the Radius of cone apex

Apollo and Case 1

The difference of the configuration between the Apollo and Case 1 is the radius of the cone apex. Little difference of the aerodynamic characteristics is observed for the base entry as expected.

Effect of the Shoulder radius

Apollo and Case 2a

The shoulder radius has significant effect on the aerodynamic characteristics for the base entry as can be seen in Figs. 14 and 15. $(C_L)_{max}$ for the Case 2a is approximately half as compared to that of the Apollo. The computed pressure distributions and the near-surface streamlines are shown in Figs. 28 and 29 for each geometry. The separation line is fixed at the shoulder for the Apollo because of the small shoulder radius as shown in Fig. 28. On the other hand, the separation line is not fixed at the shoulder for the Case 2a as shown in Fig. 29. Thus, high-pressure region appears on the base surface (area: D-A-B in Fig. 28) in case of the Apollo and this region creates high lift.

In the Case 2a, on the other hand, there exists a high-pressure region that generates the down-force (area: O1-D, direction F_d in Fig. 29). This is the main reason of the small C_L in the Case 2a. In both cases, the base region mainly creates lift, and thus, C_L takes its peak value around $\alpha = 135^\circ$ as shown in Figs. 22(b) and 24(b). The angle of the flow direction against the base surface is 45° at this attack angle. C_D for the Case 2a is smaller than that of the Apollo between $\alpha = 140^\circ$ and 180° at $M = 0.9$ and 1.2 (Figs. 14(b) and 15(b)). In the Case 2a, the pressure level behind the body is high as compared to that of the Apollo due to the large shoulder radius, resulting in the small magnitude of CA in the Case 2a as shown in Figs. 18(a) and 19(a). This is the main reason for small C_D in the Case 2a. C_D for the Case 2a is plotted in Fig. 24(a) for each Mach numbers. There exists a significant Mach number dependency in the C_D variations, although Mach number dependency are small for the Apollo as shown in Fig. 22(a). This is mainly due to the complicated separation flow and the pressure level variation behind the body. In the transonic flows, there occur local shock waves near the separation point. The appearance of local shock waves changes the C_D characteristics at transonic flow regime. Note that there occurs flow unsteadiness both in the computations and experiments in the transonic regime. Effect of shoulder radius on the C_{ma} is observed in Figs. 14(c) and 15(c). In case of the Apollo, the magnitude of the C_{ma} is very small around $\alpha = 180^\circ$. In the Case 2a, the pressure distribution on the surface changes in the axial direction with the angle of attack due to the large shoulder radius as shown in Fig. 29, resulting in the difference of the pitching moment characteristics.

Effect on C_{D0} (Case 3, 3a-1 ~ 3a-4)

Effect of the shoulder radius on the C_{D0} ($\alpha = 180^\circ$) is also investigated for the four configurations, Case

3a-1 ~ 3a-4. Radius of the cone apex R_f , diameter of the base sphere R and the cone half-angle are same as those of Case 3a. Other parameters are shown in Table 3. The shoulder radius of Case 3a-1, 3a-2, 3a-3 and 3a-4 are 2, 3, 4 and 5 times larger than that of the Case 3a. Flow conditions are shown in Table 8, and the computed C_{D0} are shown in Fig. 30(a). The averaged pressure P_{ave} working on the *surface:S1* behind the body is plotted against Mach numbers in Fig. 30(b). *Surface:S1* is defined as shown in the same figure. P_{ave} for all the configurations rapidly decreases linearly until the freestream becomes supersonic. If the freestream becomes supersonic, P_{ave} still continues decrease and its variation becomes gradual. The variation of the C_{D0} against Mach numbers is strongly related to the variation of the P_{ave} . In addition, C_{D0} is small at all Mach numbers for the configuration which has the large shoulder radius. C_{D0} decreases by roughly 0.05 ~ 0.1 when shoulder radius becomes two times larger. In total, the shoulder radius has strong effect on the lee-side pressure distributions so that the aerodynamic force changes especially in the axial direction.

Table 7: Flow conditions.

M	0.7, 0.9, 1.2, 2.0
Re	1.0×10^6
	0, 15, 24, 36, 45, 60, 70, 80, 90, 100, 110, 120, 130, 144, 156, 165, 180°

Table 8: Flow conditions for Case 3a-1 ~ 3a-4.

M	0.70, 0.90, 0.95, 1.05, 1.10, 1.20, 1.50, 2.00
Re	1.0×10^6
	180.0°

Effect of the Fineness ratio (cone half-angle)

Apollo and Case 3a

As Apollo and Case 3a have the same base geometry, the aerodynamic characteristics between $\alpha = 140$ and 180° is estimated to be similar. Effect of the lee-side configuration on the aerodynamic characteristics appears as the angle of attack decreases.

As the cone half-angle is small in the Case 3a, aerodynamic characteristics of the Case 3a tend to be influenced by the lee-side configuration at earlier angle of attack. The influence tends to come out earlier when the Mach number is high. The computed pressure distributions for the Apollo and the Case 3 at $M = 1.2$, $\alpha = 144^\circ$ are shown in Figs. 31(a) and 31(b). In both cases, high-pressure region appears on the cone part due to the freestream. Since the pressure level of the Case 3a is higher than that of the Apollo, down-force in this high-pressure region is larger for the Case 3a resulting in smaller C_L . The magnitude of the C_{ma} begins to increase rapidly at $\alpha = 144^\circ$ for $M = 0.9$ (Fig. 14(c)) and at $\alpha = 156^\circ$ for $M = 1.2$ (Fig. 15(c)), as the down-force on the lee-side surface creates large pitching moment. C_D of the Case 3a is larger than that of the Apollo between $\alpha = 90$ and 136° as shown in Figs. 14(b) and 15(b). This occurs mainly due to the difference of the area of the projection. The area of the projection is plotted for each configurations in Fig. 32. The area of the projection for the Apollo has minimum value at $\alpha = 90^\circ$, however, that for Case 3a at $\alpha = 90^\circ$ is 30 percents larger than that for Apollo at $\alpha = 180^\circ$.

Summary of the Base entry aerodynamics

Effects of the configuration parameters on the base entry aerodynamic characteristics are summarized below.

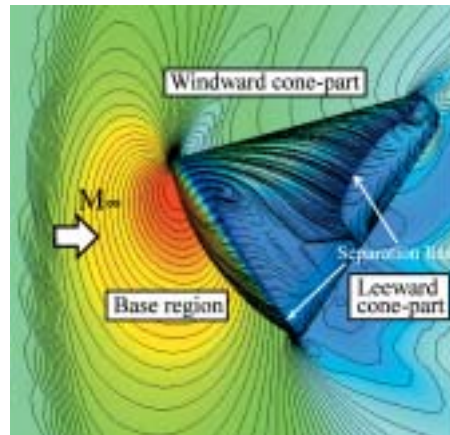


Figure 11: The structure of flow-field for Case 3b $M = 1.2$, $\alpha = 144^\circ$.

Radius of the cone apex

Radius of the cone apex has little effects.

Shoulder radius

Low C_L (L/D).

Strong Mach number dependencies of the aerodynamics.

Pressure level behind the body decreases with shoulder radius, resulting in decrease of C_{D0} .

Fineness ratio

Low C_L (L/D).

Large C_{ma} .

Different C_L and C_D characteristics.

3.2.2 Nose entry aerodynamics($\alpha = 0 \sim 90^\circ$)

Effect of the Radius of cone apex

Apollo and Case 1

C_A and C_N characteristics for the Apollo and Case 1 are shown in Fig. 27(a). C_A variations for the Apollo and the Case 1 are almost same at $M = 1.2$ but some difference is observed at $M = 0.9$. Little difference is observed in the C_N variations at $M = 0.9$ and 1.2. This indicates that C_N is not sensitive for the change of the radius of the cone apex. The radius of the cone apex has little effect on the C_{ma} at $M = 0.9$ and 1.2 as shown in Fig. 27(b).

Effect of Shoulder radius

Apollo and Case 2

The effect of the shoulder radius on the nose entry aerodynamic characteristics is expected to be small and therefore is not discussed.

Effect of the Fineness ratio (cone half-angle)

Apollo and Case 3a

Effect of the fineness ratio exists both in the C_L and C_D variations at all the angles of attack, from $\alpha = 0$ to 90° as shown in Figs. 14 and 15. C_L for the Case 3a is about three times larger than that for the Apollo between $\alpha = 0$ and 40° . High-pressure region is generated on the windward surface behind the strong detached shock wave as shown in Fig. 33(c) (area: B-C direction: F2), and the pressure component to the lift is larger than that of the Apollo due to its small cone half-angle (Apollo: 33° , Case 3a: 21°). This is the main reason for the large C_L in the Case 3a. Variation of the C_L against the angles of attack is almost linear in the Case 3a. On the other hand, the C_L for the Apollo has strong dependency on the Mach number, which is non-linear between $\alpha = 0$ and 40° (Figs. 14(a) and 15(a)).

The computed surface pressure distributions in the symmetry plane for the Apollo at the condition of base entry $\alpha = 156^\circ$ and nose entry $\alpha = 24^\circ$ are shown in Figs. 34(a) and 34(b), all the pressure distributions are normalized by the stagnation pressure p_0 . As shown in Fig. 34(a), the lee-side pressure distributions are constant (region: A-B and D-A; cone and cone-apex part) and decrease with the Mach number, while the windward pressure distributions are constant and do not change with the Mach number. There exist little Mach-number dependencies of the aerodynamic characteristics for the base entry conditions. On the other hand, for the nose entry conditions, the pressure distributions change not only in the lee-side base-region (region: A-B and D-A) but also in the lee-side cone-part (C-D) as shown in Fig. 34(b). In addition, the pressure level in the lee-side cone-part strongly depends on Mach numbers. The aerodynamic characteristics at the nose entry conditions, therefore, have high Mach number dependency. In the Case 3a, C_L in supersonic flow becomes smaller than that for the subsonic and transonic flows. The pressure distributions on the body surface in the symmetric plane are shown in Fig. 35 (The A-D shown in Fig. 33(c)). The pressure level in the base region B-A-D for $M = 1.2$ is significantly low as compared to that for $M = 0.9$. As a result, C_L for $M = 1.2$ becomes lower than that for $M = 0.9$ (Figs. 14(a) and 15(a)). There exist large difference between the variation of C_D for the Case 3a and the Apollo at $M = 1.2$ as shown in Fig. 15(a). This can be explained by the Newtonian Impact theory, and there exists the difference of the area of the projection and the direction of the normal vector of the surface to a freestream. Figure 32 shows that the projection area for the Apollo has minimum value at $\alpha = 90^\circ$. On the other hand, Case 3a has a maximum value at $\alpha = 90^\circ$ and is 30 % larger than that for the Apollo at $\alpha = 0^\circ$. Effect of the fineness ratio can be clearly observed in the C_{ma} characteristics shown in Figs. 14(c) and 15(c). In the Case 3a, the magnitude of the C_{ma} is two times larger than that of the Apollo in both conditions of $M = 0.9$ and 1.2 . In the Case 3a, the magnitude of the CN is large due to the small cone half-angle, and specific arm length for pitching moment is longer compared to that for the Apollo. These are main reasons for the large C_{ma} for Case 3a.

Effect on the C_{D0} (Apollo, Case 5, 3b, 6)

Effects of the fineness ratio on the $C_{D0}(\alpha = 0^\circ)$ characteristics are also investigated for the four types of configurations, Apollo, Case 5, 3b and 6. Radius of the cone apex R_f , diameter of the base sphere R and the shoulder radius r_s are same as those of Apollo. Other parameters are shown in Table 4. Flow conditions used in the computations are shown in Table 9. C_{D0} for all the configurations rapidly increase until the freestream becomes supersonic as shown in Fig. 36(a). Once the freestream becomes supersonic, C_{D0} takes its peak value and begins to decrease gradually with the Mach numbers. The Mach number for the peak C_{D0} depends on the fineness ratio of the body (Apollo : $M = 1.4$, Case 5 : $M = 1.2$, Case 3b : $M = 1.15$ and Case 6 : $M = 1.10$). The result indicates that the C_{D0} takes its peak value earlier for the configuration with the large fineness ratio. In addition, C_{D0} becomes large in all the Mach numbers for the configuration which has the small fineness ratio, C_{D0} increases by roughly 0.1 at subsonic conditions, 0.2 at supersonic conditions when cone half angle increases by 6° . The pressure distributions p/p_0 are shown in Figs. 37(a)-37(d) for the Apollo and the Case 3b. As shown in Figs. 37(a) and 37(b), the pressure level decreases in the base-region with Mach number and

increases in the windward region for the Apollo and the Case 3b when the flow is subsonic. Some is true for the supersonic flows as shown in Figs. 37(c) and 37(d). There exist little difference of the pressure level of the base-region between the results for the Apollo and the Case 3b. There exists significant fineness ratio effect on the pressure distributions of the windward region. The pressure level for the Apollo is larger than that for the Case 3b and that the main reason for the large C_{D0} for the Apollo.

Table 9: Flow conditions for Apollo, Case 5, 3b,

M	0.70, 0.90, 0.95, 1.05, 1.10, 1.20, 1.50, 2.00
Re	1.0×10^6
	0.0°

Summary of the Nose entry aerodynamics

Effects of the configuration parameters on the nose entry aerodynamic characteristics are summarized below.

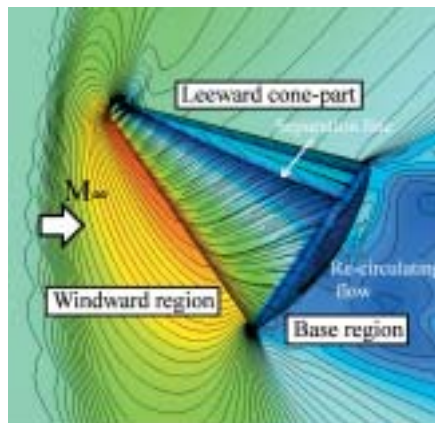


Figure 12: The structure of flow-field for Case 3b $M = 1.2$, $\theta = 36^\circ$.

Radius of the cone apex

C_A characteristics changes only when the flow is subsonic, which increase with radius of the cone apex.

C_N characteristics is not sensitive for radius of the cone apex.

Shoulder radius

Shoulder radius has little effects on the nose entry aerodynamics when $0^\circ < \theta < 60^\circ$.

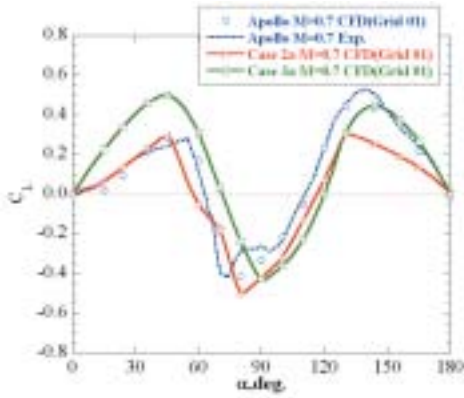
Fineness ratio

High C_L (L/D).

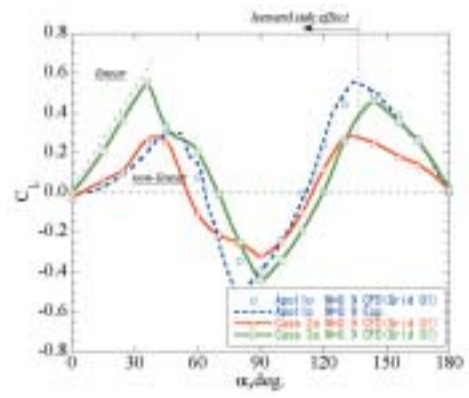
Large C_{ma} .

Different C_L and C_D characteristics.

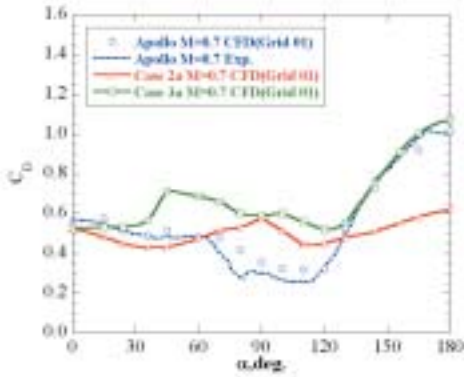
C_{D0} increases by roughly 0.1 at subsonic conditions, 0.2 at supersonic conditions when cone half-angle increases by 6°



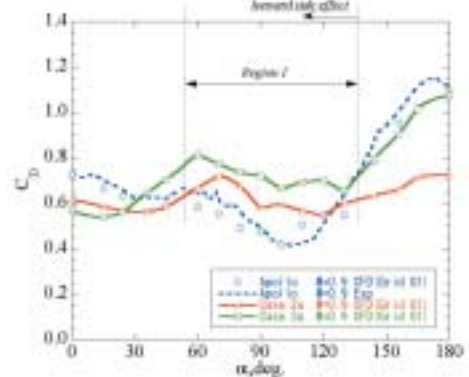
(a) Lift coefficients.



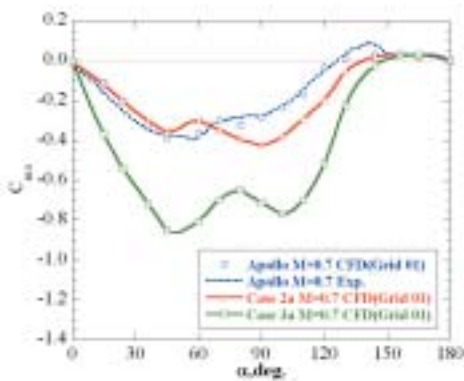
(a) Lift coefficients.



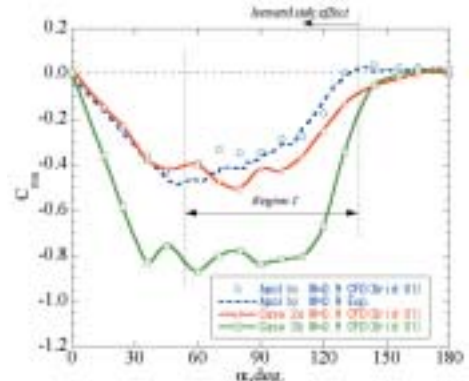
(b) Drag coefficients.



(b) Drag coefficients.



(c) Pitching moment coefficients.



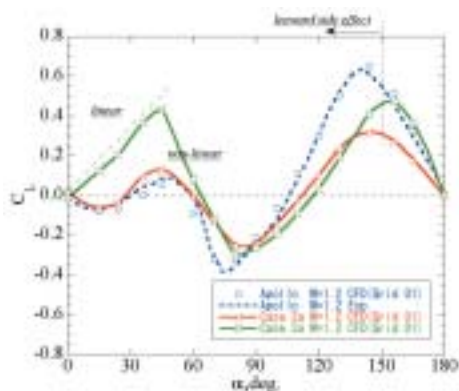
(c) Pitching moment coefficients.



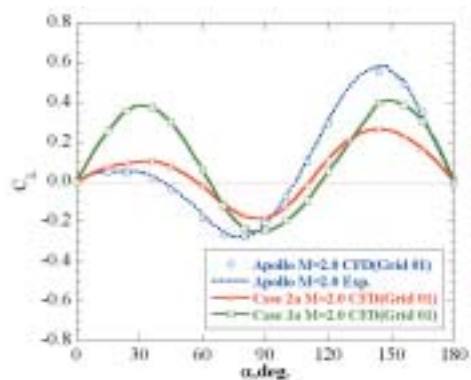
Figure 13: Computed aerodynamic coefficients for Apollo and the similar configurations at $M = 0.7$.



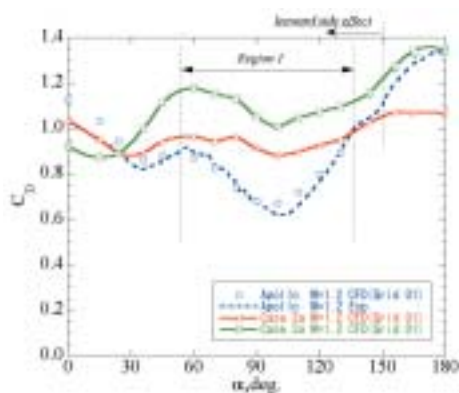
Figure 14: Computed aerodynamic coefficients for Apollo and the similar configurations at $M = 0.9$.



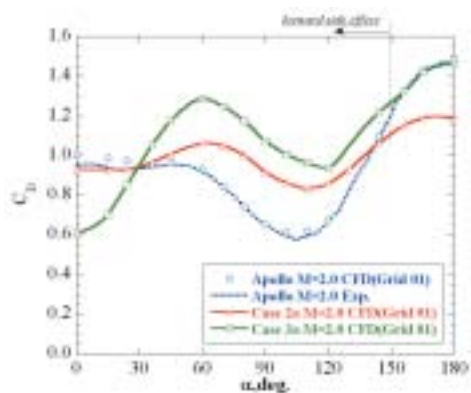
(a) Lift coefficients.



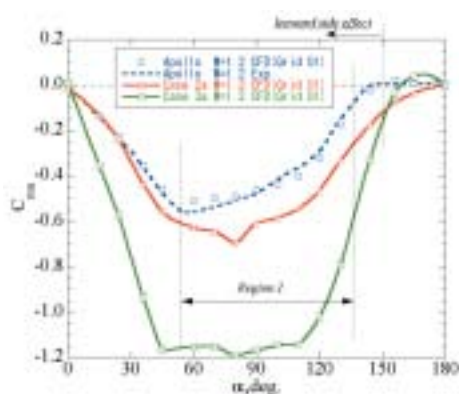
(a) Lift coefficients.



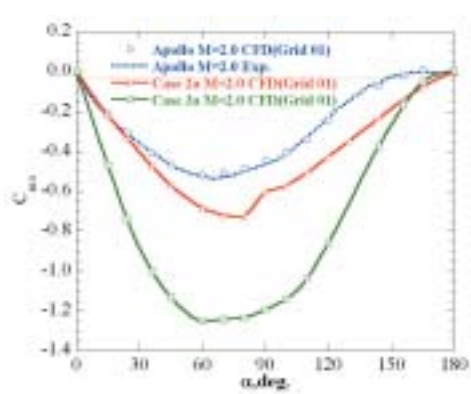
(b) Drag coefficients.



(b) Drag coefficients.



(c) Pitching moment coefficients.



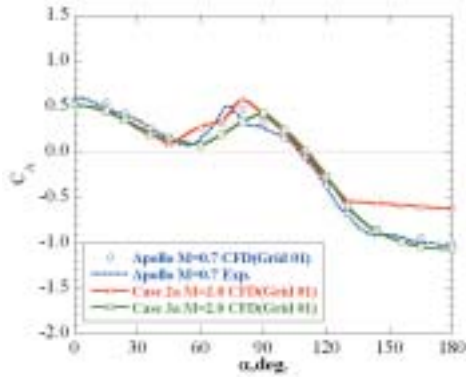
(c) Pitching moment coefficients.



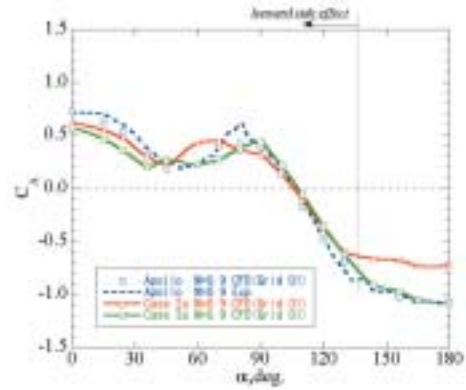
Figure 15: Computed aerodynamic coefficients for Apollo and the similar configurations at $M = 1.2$.



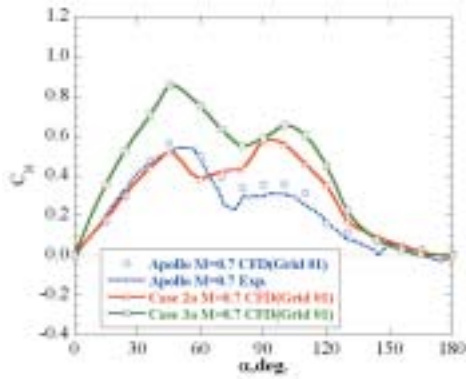
Figure 16: Computed aerodynamic coefficients for Apollo and the similar configurations at $M = 2.0$.



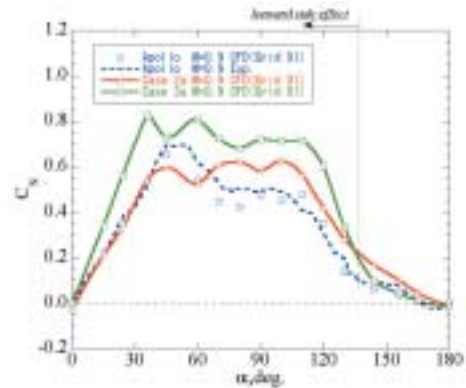
(a) Axial force coefficients.



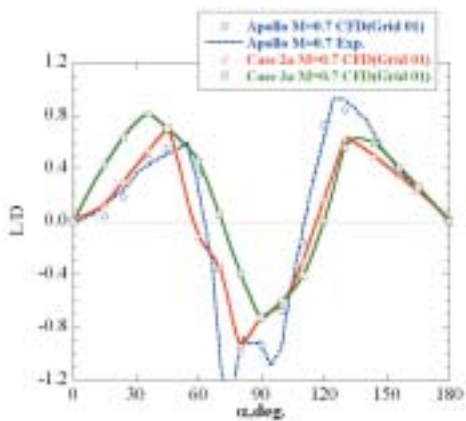
(a) Axial force coefficients.



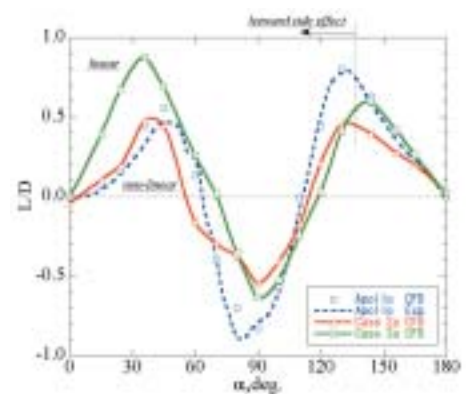
(b) Normal force coefficients.



(b) Normal force coefficients.



(c) Lift to drag ratio.



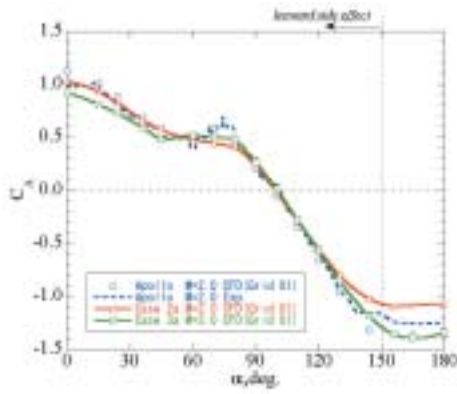
(c) Lift to drag ratio.



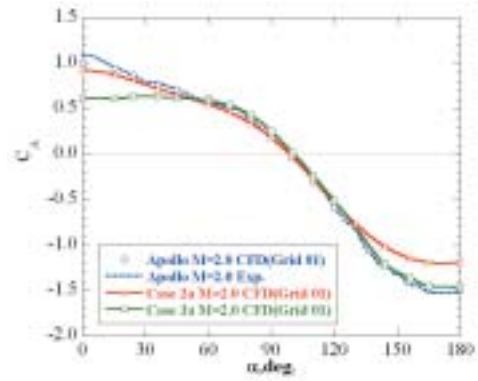
Figure 17: Computed aerodynamic coefficients for Apollo and the similar configurations at $M = 0.7$.



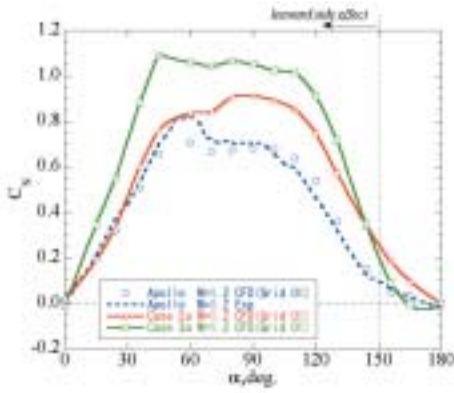
Figure 18: Computed aerodynamic coefficients for Apollo and the similar configurations at $M = 0.9$.



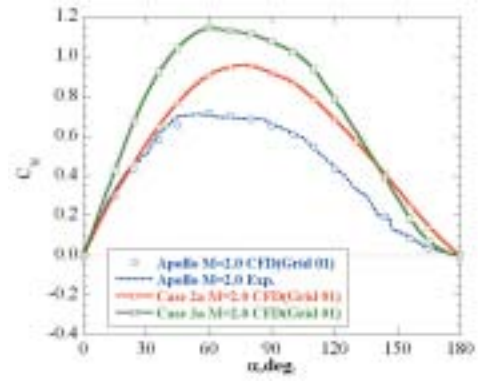
(a) Axial force coefficients.



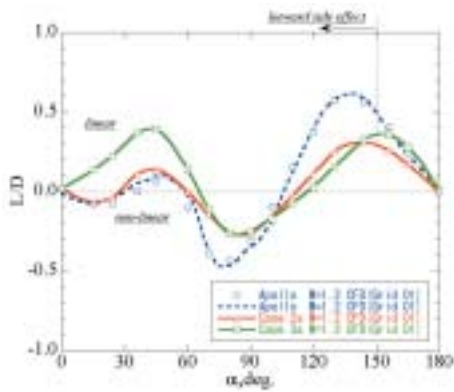
(a) Axial force coefficients.



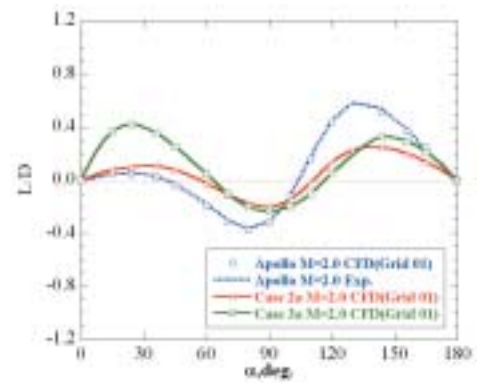
(b) Normal force coefficients.



(b) Normal force coefficients.



(c) Lift to drag ratio.



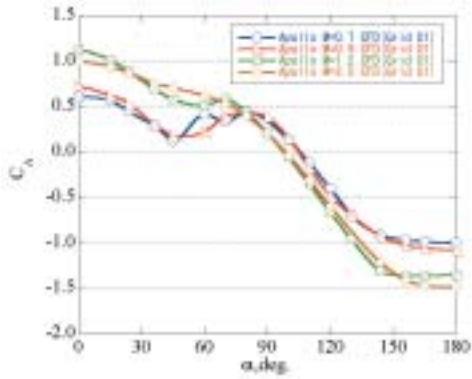
(c) Lift to drag ratio.



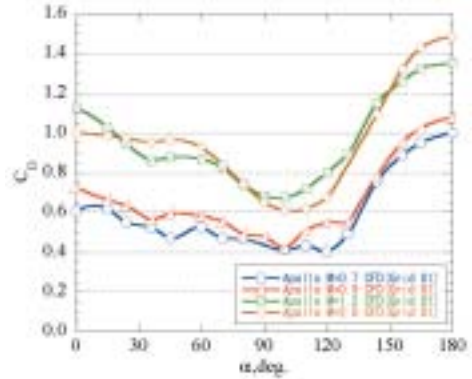
Figure 19: Computed aerodynamic coefficients for Apollo and the similar configurations at $M = 1.2$.



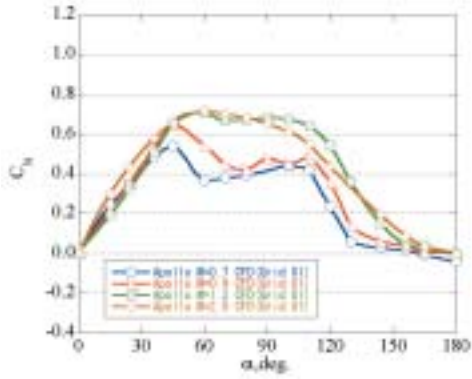
Figure 20: Computed aerodynamic coefficients for Apollo and the similar configurations at $M = 2.0$.



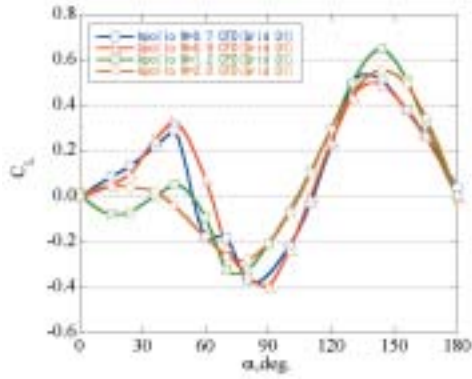
(a) Axial force coefficients C_A .



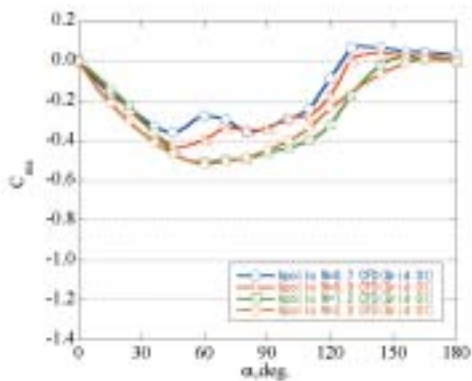
(a) Drag coefficients C_D .



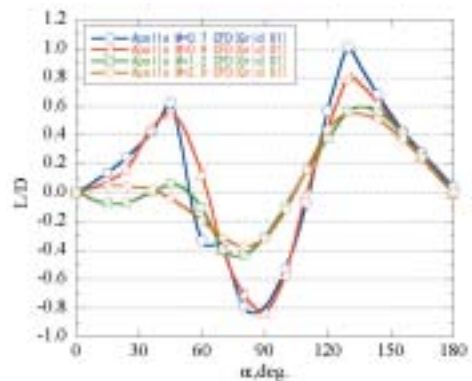
(b) Normal force coefficients C_N .



(b) Lift coefficients C_L .



(c) Pitching moment coefficients C_{ma} .



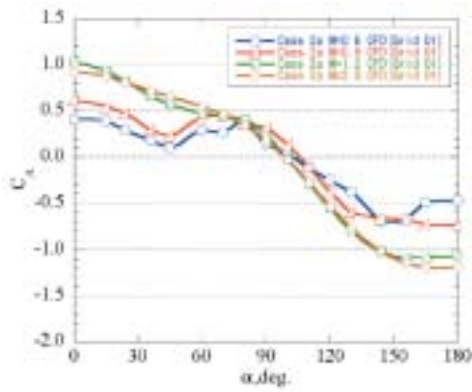
(c) Pitching moment coefficients C_{ma} .



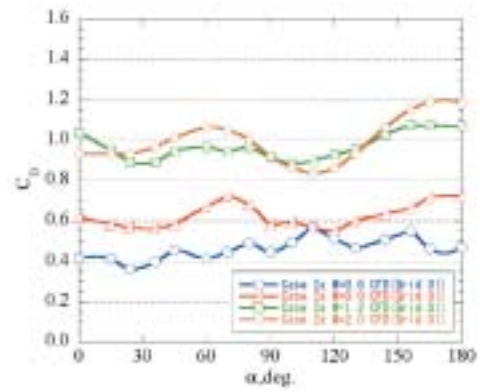
Figure 21: Computed aerodynamic coefficients for Apollo.



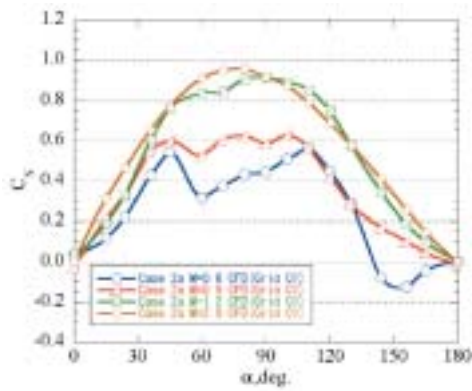
Figure 22: Computed aerodynamic coefficients for Apollo.



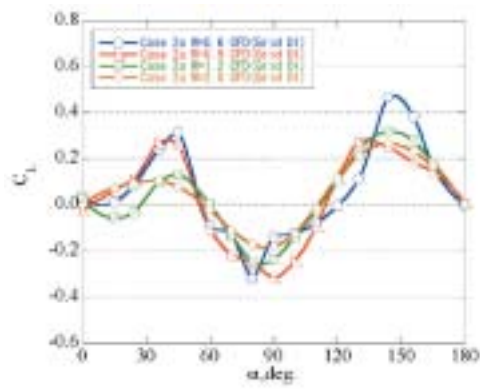
(a) Axial force coefficients C_A .



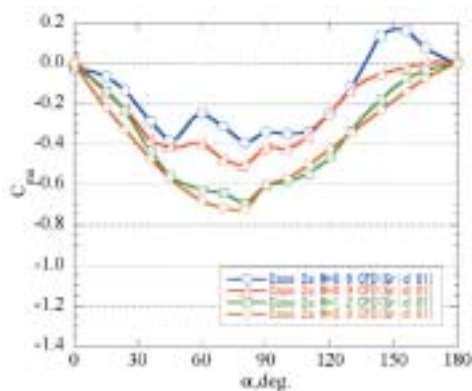
(a) Drag coefficients C_D .



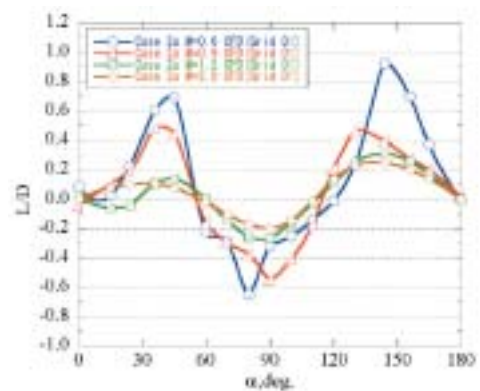
(b) Normal force coefficients C_N .



(b) Lift coefficients C_L .



(c) Pitching moment coefficients C_{ma} .

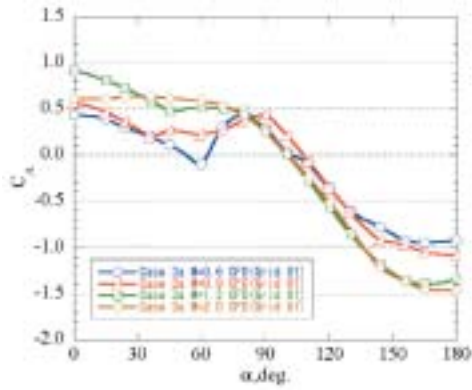


(c) Pitching moment coefficients C_{mD} .

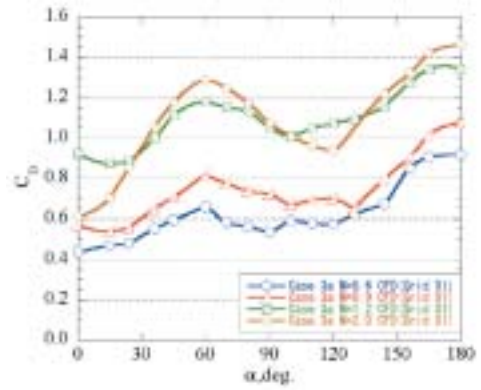


Figure 23: Computed aerodynamic coefficients for Case 2a.

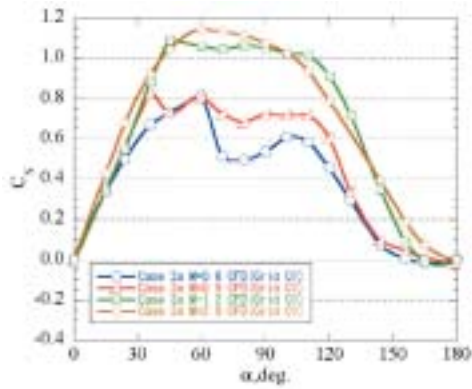
Figure 24: Computed aerodynamic coefficients for Case 2a.



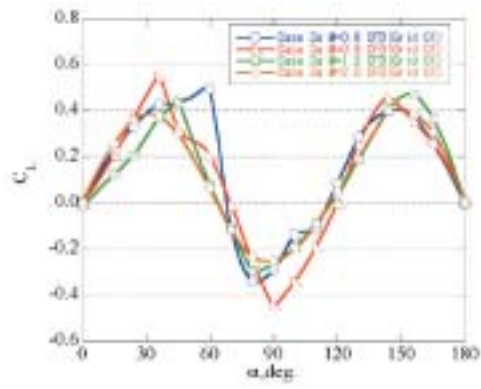
(a) Axial force coefficients C_A .



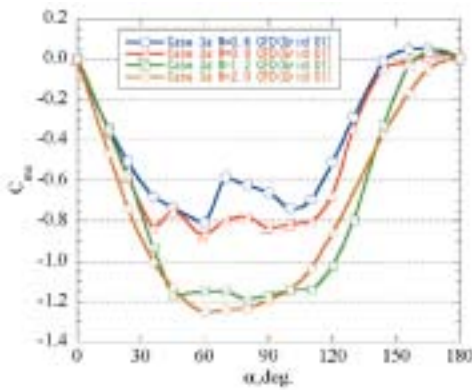
(a) Drag coefficients C_D .



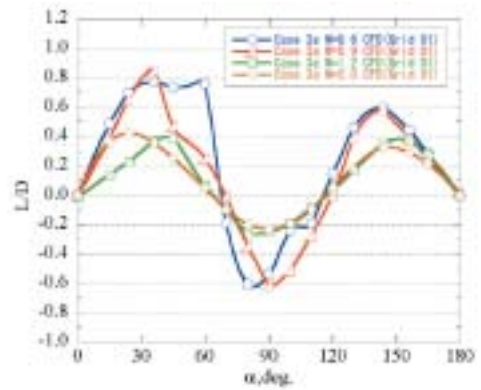
(b) Normal force coefficients C_N .



(b) Lift coefficients C_L .



(c) Pitching moment coefficients C_{ma} .



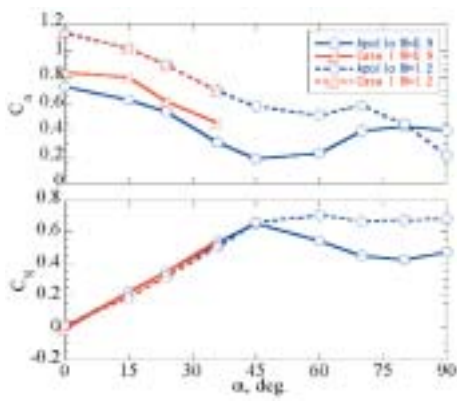
(c) Pitching moment coefficients C_{ma} .



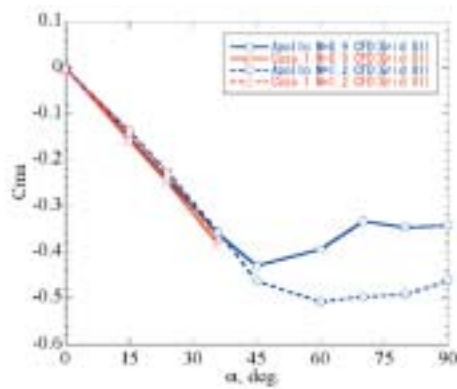
Figure 25: Computed aerodynamic coefficients for Case 3a.



Figure 26: Computed aerodynamic coefficients for Case 3a.



(a) Axial force and normal force coefficients C_A, C_N .



(b) Pitching moment coefficients C_{ma} .

Figure 27: Computed aerodynamic coefficients for Apollo and the Case 1.

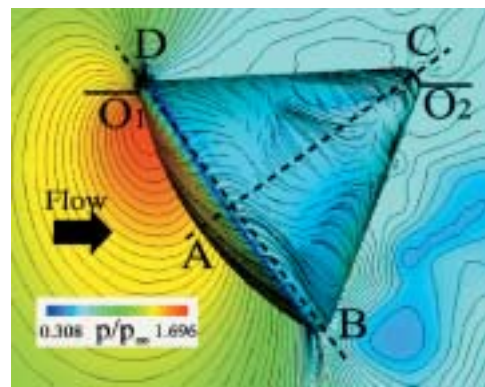


Figure 28: Computed pressure p/p_∞ distributions and surface flow pattern for Apollo at $M = 0.9, \alpha = 144^\circ$.

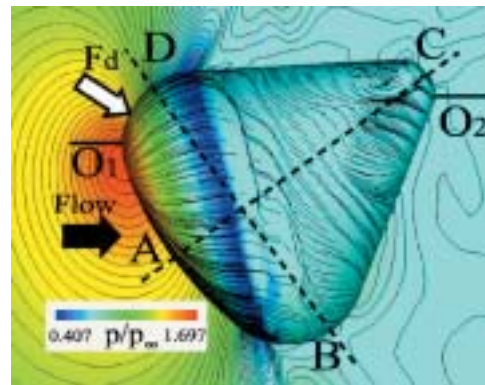
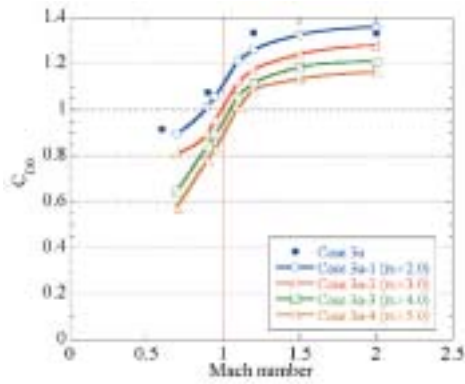


Figure 29: Computed pressure p/p_∞ distributions and surface flow pattern for Case 2 at $M = 0.9, \alpha = 144^\circ$.



(a) Computed C_{D0} for Case 3a-3d.

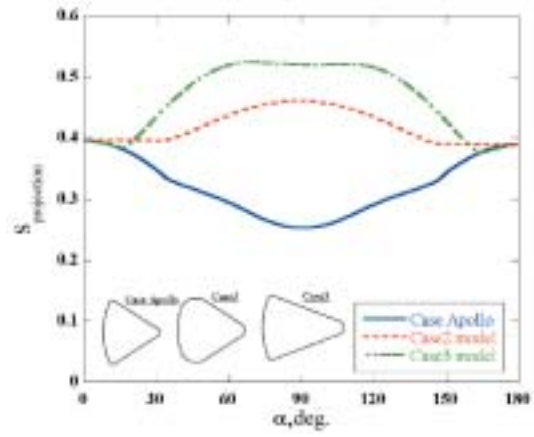
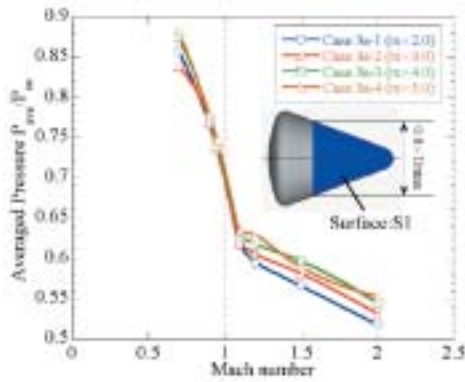
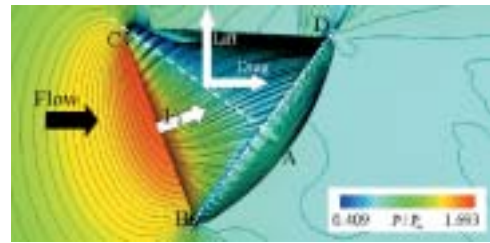


Figure 32: Area of the projection for each configurations.

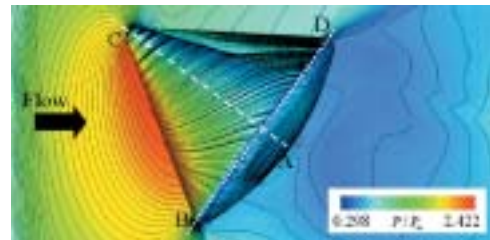


(b) Normal force coefficients C_N .

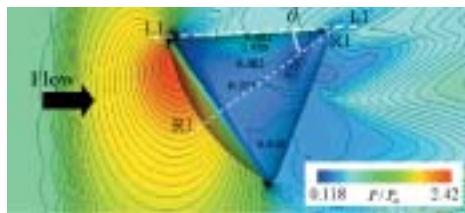
Figure 30: Averaged leeward side pressure for Case 3a-3d at $\alpha = 180^\circ$.



(a) Apollo $M = 0.9$ $\alpha = 36^\circ$.



(b) Apollo $M = 1.2$ $\alpha = 36^\circ$.

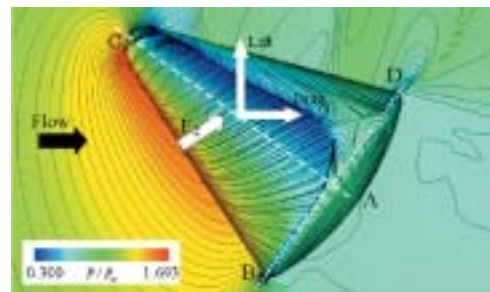


(a) Apollo $M = 1.2$ $\alpha = 144^\circ$.



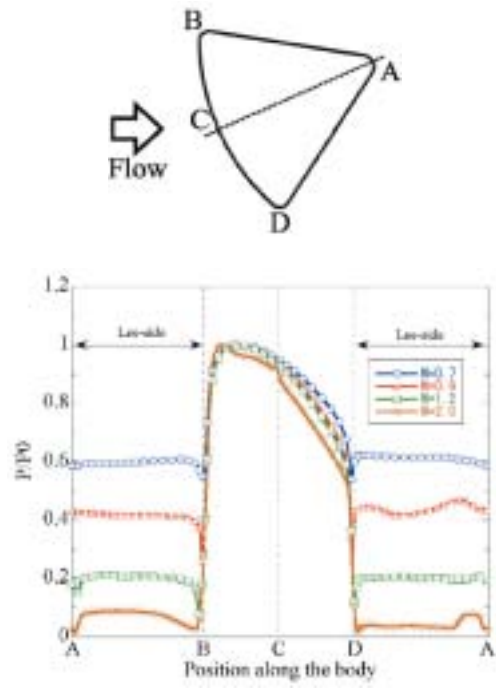
(b) Case 3 $M = 1.2$ $\alpha = 144^\circ$.

Figure 31: Computed pressure distributions p/p_∞ .

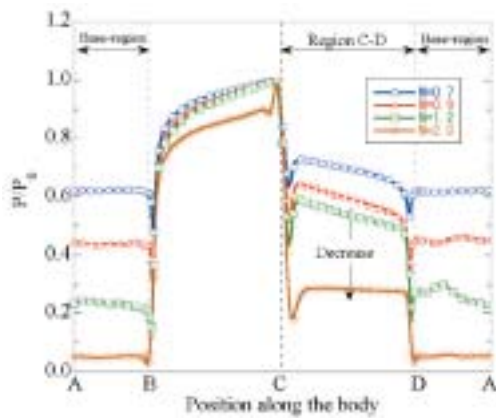
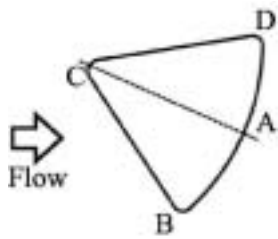


(c) Case 3a $M = 0.9$ $\alpha = 36^\circ$.

Figure 33: Computed pressure distributions p/p_∞ and surface flow pattern.



(a) Pressure distributions at $\theta = 156^\circ$.



(b) Pressure distributions at $\theta = 24^\circ$.

Figure 34: Computed pressure distributions p/p_0 in the symmetric plane for Apollo.

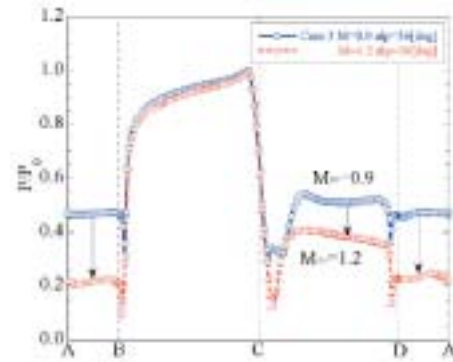
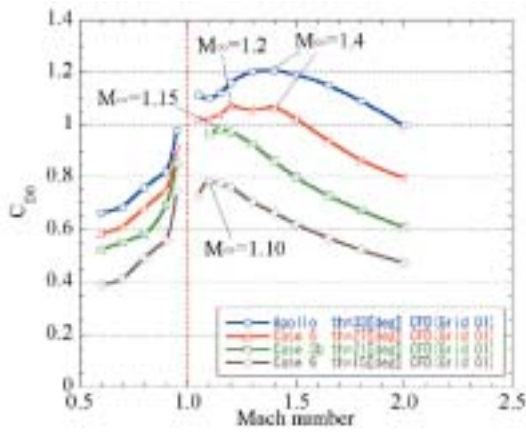
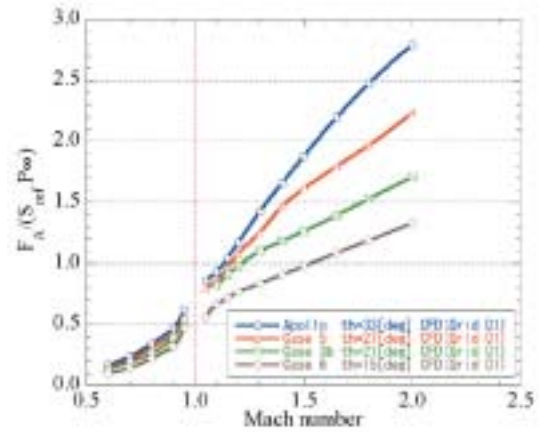


Figure 35: Computed pressure distributions for Case 3a at $\theta = 36^\circ$ $M = 0.9, 1.2$.

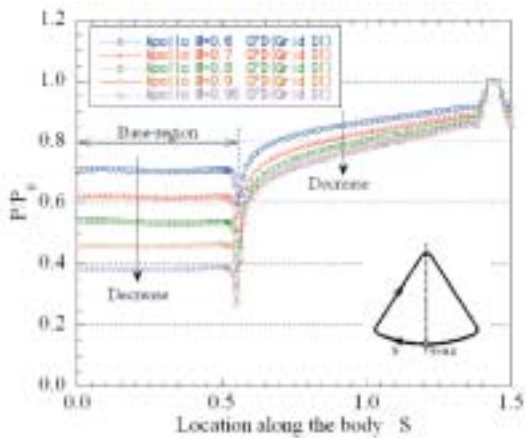


(a) C_{D0} variations against M .

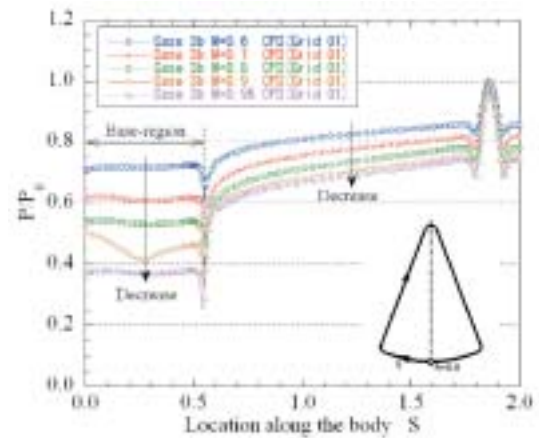


(b) $FA/(S_{ref} P_0)$ variations against M .

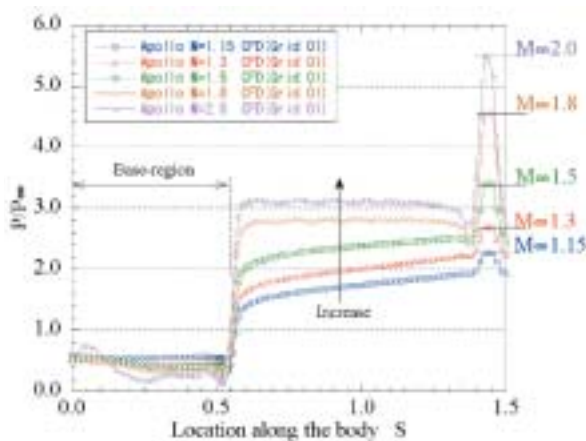
Figure 36: Body fineness effect on the aerodynamic characteristics at $\alpha = 0^\circ$.



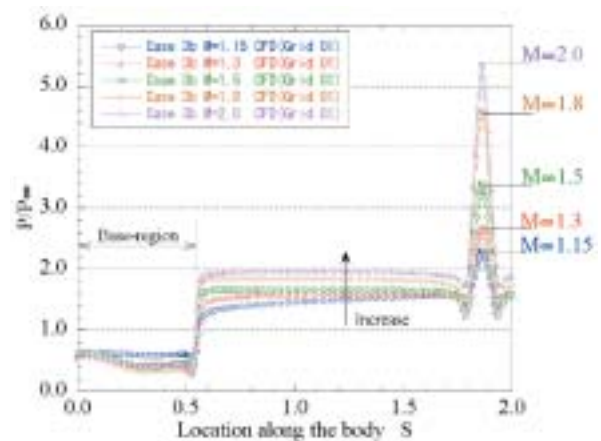
(a) P/P_0 for Apollo at subsonic condition.



(b) P/P_0 for Case 3b at subsonic condition.



(c) P/P_0 for Case 3b at supersonic condition.



(d) P/P_0 for Case 3b at supersonic condition.

Figure 37: Pressure distributions along the body for Apollo, Case 3b $\alpha = 0^\circ$.

4 Summary and Conclusions

CFD capability for the aerodynamic estimation of the basic SSTO-rocket configurations were investigated and discussed. The computed aerodynamic data for the Apollo and Apollo-like configurations showed good agreement with the experiments. CFD aerodynamic analysis can be considered to be sufficiently reliable for the preliminary design stage of the vehicle configuration.

Effects of the configuration parameters on the aerodynamic characteristics were numerically investigated. Radius of the cone apex influences only on the C_A when the flow is subsonic or transonic and has little effect on the C_N and C_{ma} .

The shoulder radius strongly influences on the position of the separation line and the lee-side pressure level so that the aerodynamic characteristics significantly changes. The separation line is not fixed at the shoulder having large radius and the local shock wave appears near the separation point at the transonic conditions resulting in the strong Mach number dependencies of the aerodynamic characteristics at the base entry conditions.

High pressure region appears on the cone surface due to the small cone half-angle on the conditions that the fineness ratio is large at base entry. The down-force is generated in this region resulting in small C_L as compared to that for the body which has the smaller fineness ratio. On the other hand, at the nose entry conditions C_L becomes larger as the aerodynamic force working on the wind-side mainly contributes to the lift. C_{ma} becomes larger in both the conditions as the specific arm length becomes longer. The fineness ratio has little effect on the lee-side pressure level but significant effect on the wind-side pressure level at $\alpha = 0^\circ$.

5 Database of Aerodynamic characteristics

All aerodynamic data are available from http://flab.eng.isas.ac.jp/ssto_aero/.

References

- [1] " Access to Space Study, Summary Report, "NASA TM-109693, 1994.
- [2] Inatani, Y., Naruo, Y., Yonemoto, K., " Concept and Preliminary Flight Testing of Fully Reusable Rocket Vehicle, " Journal of Spacecraft and Rockets, 38, No. 1,36-42(2001).
- [3] Shima E. and Jounouchi T., " Role of CFD in Aeronautical Engineering (No14) -AUSM type Upwind Schemes-, " Proceedings of the 14th NAL Symposium on Aircraft Computational Aerodynamics , pp. 7-12., 1997.
- [4] van Leer, B., " Toward the ultimate Conservative Difference Scheme.4, "Journal of Computational Physics, 23, 276-299(1977).
- [5] Fujii, K., " Practical Applications of New LU-ADI Scheme for the Three-Dimensional Navier-Stokes Computation of Transonic Viscous Flows ", AIAA Paper 86 0513, 1986.
- [6] Baldwin B. and Lomax H., " Thin Layer Approximation and Algebraic Model for Separated Turbulent Flows, "AIAA Paper 78-257,Jan, 1978.
- [7] Degani, D. and Schiff, L.B., " Computation of Turbulent Supersonic Flows around Pointed Bodies Having Cross-flow Separation, "Journal of Computational Physics, 66,173-196(1986).
- [8] Spalart, P. R., and Allmaras, S. R., " A One-Equation Turbulence Model for Aerodynamic Flows, "AIAA Paper92-0439,Jan., 1992.
- [9] Spalart, P. R., " Strategies for turbulence modeling and simulations, "4th Int. Stmp. Eng. Turb. Modeling and Measurements , pp. 669-678. May 24-26, 1999, Corsica, France
- [10] William C. Moseley, Jr., Robert H. Moore, Jr. and Jack E. Hughes., " Stability Characteristics of the Apollo Command Module, "NASA TN D-3890, 1967.
- [11] Ernest R. Hillje., " Entry Flight Aerodynamics from Apollo Mission AS-202, "NASA TN D-4185, 1967.
- [12] Fujimoto, K., and Fujii, K., " CFD Prediction of the Aerodynamic Characteristics of Capsule-like Configurations for Future SSTO Development ", AIAA Paper 03-0912, 2003.
- [13] Fujimoto, K., and Fujii, K., " Compressible Flow Simulations over Basic Reusable Rocket Configurations ", ASME/JSME Paper FEDSM 2003-45427, 2003.

A. Grid resolution and Turbulence model dependency

The grid resolution study is carried out and the grid resolution required to resolve the flow-field for the Apollo configuration is discussed. The flow conditions are shown in Table 10, subsonic flow is considered as the discrepancy mainly existed at $M = 0.7$ in the result above. The computed results on the Grid 02 and Grid 01 are shown in Figs. 38(a)-(c). The result shows the discrepancy with the experiment is reduced and the agreement becomes good. The flow separation line moves upstream comparing with the results on the Grid 01 in the computation the Grid 02. As a result, the aerodynamic characteristics is better predicted in the computation on the Grid 02.

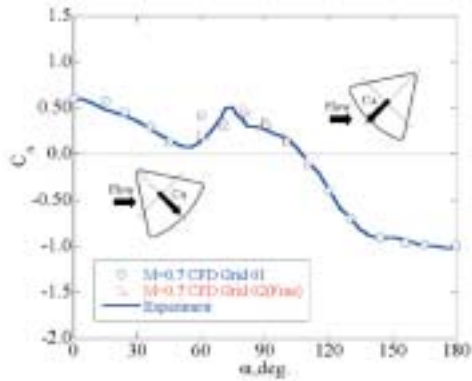
Effects of the grid resolution and the turbulence model are investigated also at the condition of $M = 0.7$, $\alpha = 0^\circ$. Since the higher grid resolution is required for the DES(Detached Eddy Simulation) analysis, effect of the turbulence model is investigated based on the results with Grid 03 using global time stepping. Time-averaged Mach number contours and stream lines limited in the symmetric plane are shown in Figs. 39 (a)-(c). Time-averaged pressure distributions in the symmetric plane are shown in Fig. 40. There exists large difference of the flow structure in the re-circulating region between the results on Grid 01 and Grid 03 with the BL model as shown in Figs. 39 (a) and (b). The stagnation point for Grid 03 moves further downstream than that for Grid 01. The re-circulation region is smaller and is located far from the body for Grid 03. As a result, the lee-side pressure level becomes higher than that on Grid 01 as shown in Fig. 40. C_A was better estimated with the fine Grid 03 as shown in Table 11. The result indicates that the CFD solutions on the coarse grid typically under-predict the leeward pressure levels, resulting in higher drag coefficients. Little difference of the flow structure is observed in the computation with the BL model and SA-DES model as shown in Figs. 39 (b) and (c). The stagnation point in the recirculation region obtained with the SA-DES is located slightly downstream as compared to that of the BL model. The stagnation point of SA-DES model is located slightly downstream comparing with the BL model. In addition, the wake flow of SA-DES model is narrower than that of the BL model. Slight improvement of the C_A prediction was obtained in the calculation with the SA-DES model as shown in Table 11.

Table 10: Flow conditions for grid resolution study.

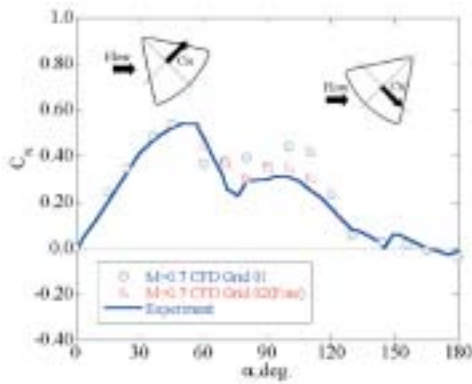
M	0.7
Re	1.0×10^6
	60, 70, 80, 90, 100, 110°

Table 11: Comparisons of computed C_A $M = 0.7$ $\alpha = 0^\circ$.

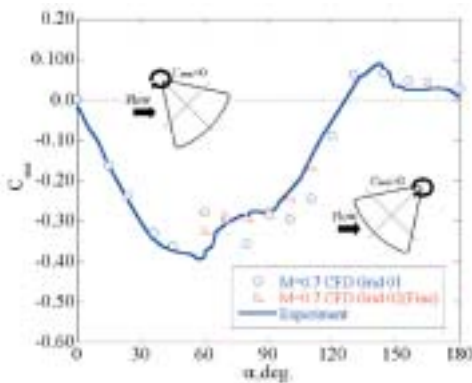
Turbulence model	Grid name	C_A
Experiment	N/A	0.6111
BL model	Grid 01	0.6864
BL model	Grid 03	0.6560
SA-DES model	Grid 03	0.6383



(a) Lift coefficients.



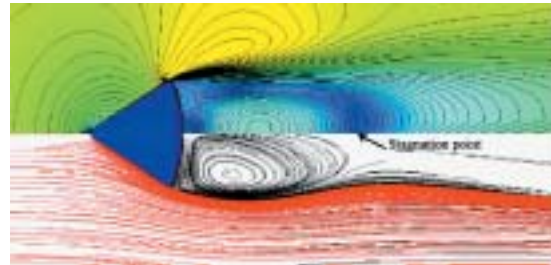
(b) Drag coefficients.



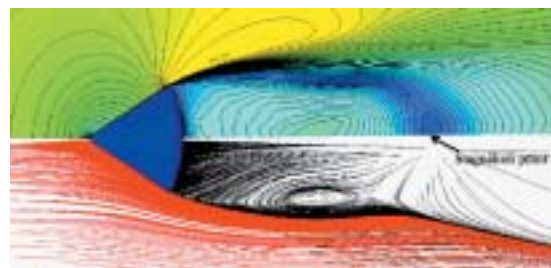
(c) Pitching moment coefficients.



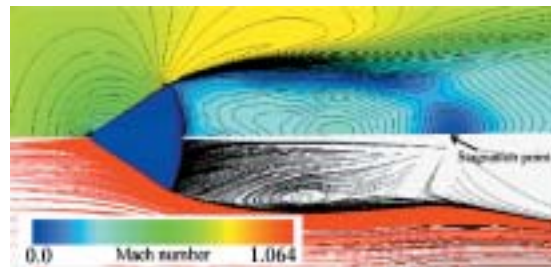
Figure 38: Grid resolution study for Apollo at $M = 0.7$.



(a) Baldwin-Lomax model (Grid 01).



(b) Baldwin-Lomax model (Grid 02).



(c) DES versions of Spalart-Allmaras model (Grid 02)

Figure 39: Mach number contours and stream line in the symmetric plane for apollo at $M = 0.7$, $\alpha = 0^\circ$.

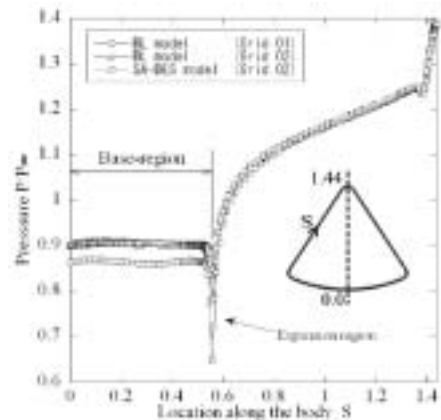


Figure 40: p/p_∞ distributions in the symmetric plane for Apollo at $M = 0.7$, $\alpha = 0^\circ$.

REPORTS ALREADY PUBLISHED

- No. 665 (March 1996)
Drago MATKO, Nobuyuki YAJIMA and Motoki HINADA: Adaptive Balloon Azimuth Control using a Simple DC Motor Actuator
- No. 666 (February 1997)
Kyoichi KURIKI, Mitsuru TAKEI, Noboru WAKASUGI and Tetsuo YASAKA: Meteoroid and Space Debris Impact Investigations in SFU Post Flight Analysis Activities: Preliminary Results and Further Directions
- No. 667 (March 1997)
Ho Sang KWAK and Kunio KUWAHARA: Transient Cooling of an Enclosed Fluid through Its Maximum-Density Temperature
- No. 668 (March 1997)
Ho Sang KWAK and Kunio KUWAHARA: Thermal Convection of an Enclosed Fluid Responding to Time-Periodic External Excitations: Effects of g-jitters and wall temperature oscillation
- No. 669 (September 1997)
Kazuhisa FUJITA and Takashi ABE: SPRADIAN. Structured Package for Radiation Analysis: Theory and Application
- No. 670 (September 1997)
Shin-ich TSUDA, Hirotaka AOKI and Takuya OKUMOTO: Nonholonomic Space Robot Path Planning for Spacecraft Attitude Stabilization and Control
- No. 671 (March 1998)
Chiyoe KOIKE and Hiroshi SHIBAI: The Infrared Spectra of Candidate Materials for Celestial Dust by Laboratory Measurements
- No. 672 (March 1999)
Takehiko KAWAHISIMA, Koichiro OYAMAMA and Katsuhisa SUZUKI: A Measurement of Vibrational-Rotational Temperature and Density of Molecular Nitrogen in the Upper Atmosphere by Rocket-Borne Electron Beam Induced Luminescence
- No. 673 (March 1999)
Tsutomu T. TAKEUCHI, Hiroyuki HIRASHITA, Kouji OHTA, Takako T. ISHII, Kohji YOSIKAWA: Simulation of the IRIS Far-infrared Survey: A Guide for Infrared Galaxy Number Counts
- No. 674 (March 1999)
Kunio KUWAHARA and Karl G. ROESNER: Shock Wave Development around Accelerated Bodies at Supersonic Mach Numbers Slightly Larger than One
- No. 675 (September 1999)
K. K. MAHAJAN and Kohichiro OYAMA: Venus Ionosphere: Major Features
- No. 676 (March 2000)
Kojiro SUZUKI, Hiroaki HIMEKI, Tadaharu WATANUKI and Takashi ABE: Experimental Studies on Characteristics of Shock Wave Propagation through Cylinder Array
- No. 677 (March 2000)
Hiroaki SHIRAIISHI, Satoshi TANAKA, Masahiko HAYAKAWA, Akio FUJIMURA and Hitoshi MIZUTANI: Dynamical Characteristics of Planetary Penetrator: Effect of Incidence Angle and Attack Angle at Impact
- No. 678 (July 2000)
K. NOGUCHI, T. IMAMURA and K.-I. OYAMA: A Feasibility Study for Observing Small Lunar and Martian Ionospheres by Radio Occultation Technique
- No. 679 (March 2001)
Takashi WATANABE, Katsuhisa SUZUKI and Koichiro OYAMA: Observation of Stratospheric Ozone with MT-135 Rockets in 1990-1999
- No. 680 (March 2001)
Yong-Chun XIE, Hideyuki SAWADA, Tatsuaki HASHIMOTO and Keiken NINOMIYA: Actively Controlled Magnetic Bearing Momentum Wheel and Its Application to Satellite Attitude Control
- No. 681 (March 2001)
Mikako MATSUURA, Takao NAKAGAWA, Hiroshi MURAKAMI and Issei YAMAMURA: A simulation code for the infrared whole sky survey with the Far-Infrared Surveyor (FIS) on board ASTRO-F

SAS